Journal of Spectroscopy

WILEY

RESEARCH ARTICLE OPEN ACCESS

Application of Near-Infrared Spectroscopy Combined With Chemometrics for the Assessment of Peimine/Peiminine Content and Antiviral Efficacy in *Fritillaria thunbergii*

Haishen Li[1] | Chuanbao Wang[1] | Minda Zhang[1] | Long Cai[1] | Zhian Wang[1,2,3] | Aimin Lv[2] | Qingsong Shao[2] | Jianming Jiang[1] | Jian Sun[1,2,3]

[1]Traditional Chinese Medicine Resources Center, Zhejiang Research Institute of Traditional Chinese Medicine Co., Ltd., Hangzhou, Zhejiang 310023, China | [2]Zhejiang Provincial Key Laboratory of Resources Protection and Innovation of Traditional Chinese Medicine, Zhejiang Agriculture and Forest University, Hangzhou 311300, China | [3]State Key Laboratory for Quality Ensurance and Sustainable Use of Dao-Di Herbs, Beijing 100700, China

Correspondence: Jian Sun (21116025@zju.edu.cn)

Received: 1 August 2025 | **Revised:** 4 December 2025 | **Accepted:** 2 January 2026

Academic Editor: Daniel Cozzolino

Keywords: antiviral activity | chemometrics | *Fritillaria thunbergii* miq. | near-infrared spectroscopy | peimine | peiminine

ABSTRACT

Fritillaria thunbergii bulbus is a traditional Chinese medicine widely used for its expectorant and antitussive effects. However, the practical application of existing detection methods is significantly limited by their complex sample preparation, lengthy experimental procedures, and stringent technical requirements. In this study, a rapid and accurate method for determining the content of peimine (PE), peiminine (PEM), and antiviral activity (AVA) in *F. thunbergii* was established using near-infrared spectroscopy (NIRS) combined with chemometrics. A total of 79 batches of samples were collected to investigate the influence of five different processing methods (including shell powder processing, sulfur fumigation, slice-drying, little-complete-drying, and freeze-drying) on quality attributes. Quantitative models were established based on the partial least squares (PLS) algorithm, with model optimization achieved through two wavelength selection methods: synergy interval partial least squares (Si-PLS) and competitive adaptive reweighted sampling (CARS). Results indicated that processing methods significantly affected PE/PEM content and AVA. Freeze-dried *F. thunbergii* demonstrated optimal performance, achieving the highest total PE/PEM content (0.1735%) and superior AVA (8.517 U/mg). The CARS-PLS model demonstrated the best performance with the coefficient of determination for prediction (R_P^2) values of 0.8850, 0.8240, and 0.8336 for PE, PEM, and AVA, respectively. The root mean square error of prediction (RMSEP) for PE, PEM, and AVA were 0.0101%, 0.0070%, and 1.7921 U/mg, respectively. The residual predictive deviation (RPD) values for all three models were greater than 2.4. These results indicate that the established model enables the rapid determination of PE, PEM content, and AVA in *F. thunbergii* and can be applied for the rapid and nondestructive discrimination of the quality of *F. thunbergii* medicinal material.

1 | Introduction

Fritillaria thunbergii bulbus (FTB) is a renowned traditional Chinese medicinal material. Its bulb, utilized as the medicinal part, exhibits pharmacological effects including heat-clearing, phlegm-resolving, antitussive, and detoxifying properties [1–4]. FTB is primarily cultivated in the southeastern coastal, central, and eastern regions of China (such as Zhejiang, Jiangsu, Anhui, and Hunan provinces) [5]. Peimine (PE) and peiminine (PEM) are identified as the principal alkaloid compounds in FTB,

This is an open access article under the terms of the Creative Commons Attribution License, which permits use, distribution and reproduction in any medium, provided the original work is properly cited.

Copyright © 2026 Haishen Li et al. *Journal of Spectroscopy* published by John Wiley & Sons Ltd.

responsible for its diverse pharmacological activities, including antitussive, anti-asthmatic [6], anti-inflammatory [7–9], and antiviral properties [10]. The Chinese Pharmacopoeia (2020 Edition) specifies the total content of PE and PEM as the chemical marker for evaluating the quality of this medicinal material [1]. However, the current standard detection method, high-performance liquid chromatography (HPLC), presents significant limitations due to its operational complexity, time-consuming nature, and reliance on toxic solvents [11–13]. This highlights an urgent need for rapid, nondestructive methods for quality assessment.

Beyond chemical composition, the biological activity of FTB is equally crucial. FTB is a commonly used medicinal herb in traditional Chinese medicine formulations for the treatment of viral influenza [1]. Notably, Kim et al. [10] demonstrated that the extract of *F. thunbergii* effectively inhibited the replication of the influenza A/H1N1 virus in cellular, chick embryo, and murine models. Compared to the neuraminidase (NA) inhibitor oseltamivir, the extract exhibited a superior safety profile at the experimental doses employed, indicating substantial potential as a novel anti-influenza candidate drug or supplementary therapy. Therefore, evaluating the antiviral activity (AVA) is essential for a comprehensive quality assessment of FTB.

Processing methods significantly impact the quality of FTB. Historically, various processing techniques have been applied to FTB, such as shell powder-processed *F. thunbergii* and sulfur-processed *F. thunbergii*. Different processing methods alter the content of bioactive components, including PE and PEM, resulting in some samples failing to meet pharmacopoeial standards [12]. However, the clinical applicability of these substandard FTB samples remains uncertain. Comparative analysis of the chemical composition and biological activity across different processing methods can provide critical guidance for optimizing the production and processing of *F. thunbergii.*

Near-infrared spectroscopy (NIRS) demonstrates significant potential for predicting the content of bioactive components and biological activity in traditional Chinese medicines [14, 15]. For instance, Du et al. [16] employed NIR spectroscopy combined with partial least squares (PLS) regression to develop quantitative models for *Rubi Fructus* using moisture content, ellagic acid, and total flavonoids as indicators. Hao et al. [17] utilized NIR to establish PLS quantitative models for the total flavonoid content (TFC), xanthine oxidase (XO) inhibitory activity, and antioxidant activity (AA) of *Prunus mume*. Zhang et al. [18] integrated NIR spectroscopy with chemometrics, adopting PLS and support vector machine (SVM) algorithms to construct calibration models with robust predictive performance for quinic acid, protocatechuic acid, and 6-hydroxykynurenic acid in *Ginkgo biloba* leaves. However, studies utilizing NIR spectroscopy for the detection of PE/PEM content and associated biological activity in *F. thunbergii* remain rarely reported.

In this study, we aimed to develop a rapid and nondestructive method for the simultaneous determination of PE, PEM content, and AVA in *F. thunbergii* using NIR spectroscopy combined with chemometrics. PE and PEM contents were quantified using validated HPLC methods, while AVA was determined with a Neuraminidase Inhibitors Screen Kit. Quantitative models were established based on the PLS algorithm, with model optimization achieved through two wavelength selection methods: synergy interval partial least squares (Si-PLS) and competitive adaptive reweighted sampling (CARS). Furthermore, we investigated the influence of various processing methods on these quality indicators. Our findings offer a valuable reference for the comprehensive and rapid quality assessment of *F. thunbergii* medicinal materials.

2 | Materials and Methods

2.1 | Samples

Seventy-nine *F. thunbergii* samples were collected from Zhejiang, China (Table 1). Samples S6–S79 were obtained as directly dried materials from production areas. Samples S1–S5 (triplicates per group) were harvested from the same plot in Xinwo Town, Pan'an County, on May 12, 2024, and processed as follows: shell powder-processed *F. thunbergii*: Fresh bulbs were selected, cored, washed, and abraded to remove the epidermis. Mixed with calcined shell powder (4 kg per 100 kg bulbs) to absorb exudates, stored overnight, then sun-dried for 3–4 days with intermittent stacking (2–3-day intervals). Sulfur-processed *F. thunbergii*: Washed bulbs in mesh bags were wrapped in nylon fabric, sulfur-fumigated (6 kg sulfur per 1000 kg material) for 24 h, and sun-dried. Little-complete-dried *F. thunbergii*: Intact fresh bulbs (height: 1–1.5 cm; diameter: 1–2.5 cm) were washed and sun-dried. Freeze-dried *F. thunbergii*: Selected, cored, and washed bulbs were prefrozen at −40°C overnight, then lyophilized in flasks at 2.4 Pa for 30 h. Slice-dried *F. thunbergii*: Harvested bulbs were washed, cored, machine-sliced, and dehydrated to constant weight (Supporting Figure S1). All samples were pulverized through an 80-mesh sieve (< 180 μm particle size) and stored in sealed bags at 4°C.

2.2 | Reagents

PE (CAS: 23496-41-5), PEM (CAS: 18056-10-4), Shanghai Yuanye Bio-Technology Co., Ltd. Acetonitrile (HPLC grade; TEDIA, USA), methanol (analytical grade), chloroform (analytical grade), phosphoric acid (85%, analytical grade; Zhejiang Chemical Co., Ltd.), peramivir trihydrate (98%, Batch S06M11H109335; Shanghai Yuanye Bio-Technology).

2.3 | Reference Analysis

2.3.1 | Chemical Determination Values of PE, PEM

Detection methods were performed with reference to the Chinese Pharmacopoeia (2020 Edition).

2.3.2 | Measurement of Antiviral Activity In Vitro

Reference standard solution preparation: Precisely weigh 8.47 mg of peramivir trihydrate, dissolve in methanol, and dilute to 25 mL to obtain the stock solution. Dilute this solution by factors of X and 1.33 X based on sample concentration and NA inhibition rate (maintained at 50%).

2.3.2.1 | Test Sample Solution Preparation. Accurately weigh 2.0 g of sieved *F. thunbergii* powder into a 50 mL stoppered conical flask. Add 30 mL of 80% (v/v) ethanol, and record the total weight. Sonicate for 45 min followed by overnight maceration. Replenish with methanol to the initial weight, then

TABLE 1 | Sample information.

Sample Id	Processing method
Y01	Shell powder-processed *Fritillaria thunbergii*
Y02	Sulfur-processed *Fritillaria thunbergii*
Y03	Slice-dried *Fritillaria thunbergii*
Y04	Little-complete-dried *Fritillaria thunbergii*
Y05	Freeze-dried *Fritillaria thunbergii*
Y06∼Y79	Dried samples were collected directly from the producing area

filter through a 0.45 μm syringe filter. Use the filtrate as the test solution.

2.3.2.2 | Assay Procedure. (a) Standard curve preparation: In a black 96-well fluorescence microplate, add 70 μL of NA assay buffer to 6 × 2 wells. Sequentially add 0, 1, 2, 5, 7.5, and 10 μL of NA solution, then supplement with Milli-Q water to adjust the total volume to 90 μL per well. (b) Sample detection setup: employ the parallel-line assay for quantitative responses (ChP 2020 Vol III, Section 1431, 2.2) to determine sample potency. Key parameters: number of dose–response replicates (m): 4; two concentration levels for standard (S) and test (T); dose ratio between adjacent concentrations (r): 0.75. Add 70 μL NA assay buffer and 10 μL NA solution to each well. Then add 10 μL of test sample solution (total volume: 90 μL/well). (c) Detection protocol: (1) vortex-mix for 1 min; (2) incubate at 37°C for 2 min; (3) add 10 μL fluorescent NA substrate per well; (4) vortex-mix for 1 min; (5) incubate at 37°C in dark for 10 min; (6) measure fluorescence intensity (excitation wavelength 322 nm, emission wavelength 450 nm); (7) calculate mean values. The standard curve was made according to the amount of NA added and the corresponding measured fluorescence intensity. Combined with the NA standard curve, the inhibition rate of different concentrations of samples on NA was calculated. The inhibition rate was calculated as inhibition rate = $(10 - M)/10 \times 100\%$, and M represents the remaining NA volume after reaction with the sample. Titer calculation: The titer of each sample was calculated according to the parallel line method (2.2) of the quantitative reaction of the 1431 bioassay statistical method in the third part of the Pharmacopoeia of the People's Republic of China 2020 Edition.

2.4 | NIR Spectra Collection

Near-infrared (NIR) spectra were collected using a Fourier transform near-infrared (FT-NIR) spectrometer (Antaris II, Thermo Fisher Scientific, USA) in diffuse reflectance mode. Approximately 2 g of powdered *F. thunbergii* sample was uniformly loaded into a circular sample cup. Spectral acquisition was performed over the wavenumber range of 4000∼10,000 cm^{-1} with a resolution of 8 cm^{-1}. Each scan accumulated 64 interferograms, and background correction was conducted using an air spectrum as a reference. To minimize heterogeneity-induced errors, triplicate measurements were performed per sample, with the averaged spectrum subsequently used for variable analysis.

2.5 | Spectral Preprocessing

Due to physical variations, irrelevant information such as background noise, instrument dark current, and particle size/shape differences interferes with raw spectra. Consequently, implementing preprocessing procedures is essential to establish stable and reliable models that effectively reduce and eliminate unnecessary spectral interference. This study employed six spectral preprocessing techniques—including first derivative, MSC, SNV, and their combinations—to mitigate baseline drift and enhance spectral contrast between samples. The first-derivative method efficiently minimizes peak overlap while eliminating constant and linear baseline shifts. MSC separates scattering signals from absorption signals using a uniform scattering coefficient, addressing both additive and multiplicative effects in spectra. SNV standardizes variables in NIR diffuse reflectance spectroscopy to attenuate slope variations and correct scattering effects.

2.6 | Optimal Wavelength Selection

Spectral data collected from samples encompass numerous variables, many of which may be irrelevant. Optimal variable selection reduces extraneous factors, thereby decreasing computational complexity and enhancing model accuracy [19]. This study employed two prevalent variable selection methods—Si-PLS and CARS—to construct more precise models. The CARS algorithm integrates Monte Carlo sampling with PLS regression coefficients, utilizing adaptive reweighted sampling (ARS) to retain wavelengths with large absolute regression coefficients while eliminating low-weight wavelengths through an exponentially decreasing function (EDF). The optimal subset is identified by minimizing the root mean square error of cross-validation (RMSECV). Compared to full-spectrum modeling, CARS offers three key advantages: significant dimensionality reduction for improved computational efficiency, elimination of redundant information to enhance predictive accuracy, and increased model interpretability for critical spectral feature analysis. Implementation involves (1) random selection of 80% samples for PLS calibration; (2) EDF-driven removal of wavelengths with small regression coefficients; and (3) ARS-based retention of high-coefficient wavelengths, culminating in selection of the subset with minimal RMSECV. Identically, Si-PLS operates by partitioning the full spectrum into intervals (e.g., 10, 20, or 30 segments) and evaluating combinations of 2–4 subintervals to exploit synergistic effects between spectral regions, thereby identifying the interval combination that delivers optimal predictive performance.

2.7 | Quantitative Analysis With PLS

PLS regression models were employed to quantify PE/PEM content and AVA in 79 batches of FTB. Regression models were established using preprocessed NIR spectral data, with the optimal preprocessing method determined by comparative evaluation of PLS model performance metrics.

2.8 | Model Performance Evaluation

The performance of the models was evaluated using six statistical metrics, in accordance with established studies [20, 21]: the coefficients of determination for calibration (R_C^2) and prediction (R_P^2), the root mean square errors of calibration (RMSEC) and prediction (RMSEP), and the residual predictive deviation for both calibration (RPDC) and prediction (RPDP). Generally, R^2 values approaching 1 and RMSE values approaching 0 indicate superior model accuracy and robustness. Furthermore, the predictive capability was assessed based on the residual predictive deviation (RPD) values. An RPD value greater than 2.0 indicates that the model prediction is reliable and can be accepted for quantitative analysis [22]. The formula is as follows [21]:

$$R^2 = 1 - \frac{\sum_{i=1}^{n}(y_i - \hat{y}_i)^2}{\sum_{i=1}^{n}(y_i - \bar{y}_i)^2},$$

$$\text{RMSE} = \sqrt{\frac{\sum_{i=1}^{n}(y_i - \hat{y}_i)}{N}}, \quad (1)$$

$$\text{RPD} = \frac{\text{SD}}{\text{RMSEP}},$$

where $y_i, \hat{y}_i$ represents the standard value and the predicted value of the sample $\bar{y}_i$ is the average value of the sample set components, N is the number of observations, and SD stands for standard deviation. When Y refers to the training set, the resultant parameters correspond to the training set. All modeling and analysis were performed using MATLAB R2023b.

To avoid model overfitting, all modeling procedures employed the full cross-validation method (leave-one-out cross-validation, LOOCV) to determine regression model parameters. Simultaneously, the maximum number of latent variables in the partial least squares regression (PLSR) model was set to 15. Through iterative screening of sample subsets, PLSR calibration models were established: Specific samples were sequentially excluded for modeling calculations, with predicted values compared against reference values. The screening scope was gradually expanded until all remaining samples were covered, while simultaneously calculating the coefficient of determination for cross-validation (R_{CV}^2) and the RMSECV. RMSECV reflects the degree of deviation between predicted and actual values, whereas R_{CV}^2 indicates the correlation between predicted and actual values [20].

3 | Results

3.1 | The PE, PEM, and AVA Results Using the Reference Methods

The PE, PEM, and AVA of the 79 samples were determined using the reference methods, and the content ranges of PE (%), PEM (%), and AVA (U/mg) are presented in supporting table S1. Obviously, significant differences in PE/PEM contents and AVA of *F. thunbergii* were observed due to processing methods. The content ranges of the reference values are 0.013∼0.165% for PE, 0.009∼0.084% for PEM, and 0.252∼36.098 U/mg for AVA (Supporting Table S1). Based on the frequency distribution plot (Figure 1), the PE content (%) was primarily observed in the range of 0.05%–0.07%, the PEM content (%) ranged from 0.03% to 0.06%, and the AVA (U/mg) was mainly distributed between 1 and 7 U/mg.

3.2 | Effect of Processing Methods on PE/PEM Content and AVA

Different processing methods significantly affect the PE/PEM content and AVA (Figure 2). Data indicate that the highest PE/PEM contents were consistently observed in freeze-dried *F. thunbergii*, followed by little-complete-dried *F. thunbergii*, slice-dried *F. thunbergii*, sulfur-processed *F. thunbergii*, and shell powder-processed *F. thunbergii*, with substantial variations among them. The PE and PEM contents in freeze-dried *F. thunbergii* were 5.31-fold and 3.54-fold higher, respectively, than those in shell powder-processed *F. thunbergii*. The AVA of shell powder-processed samples was markedly lower than that of the other four processed types, measuring less than half of their values. The highest activity was detected in freeze-dried *F. thunbergii*, reaching 8.517 U/mg.

3.3 | Cluster Analysis Based on PE, PEM, and AVA Results

Cluster analysis was performed on normalized PE, PEM, and AVA results (Figure 3). The analysis revealed a significant correlation between PE and PEM, whereas no evident correlation

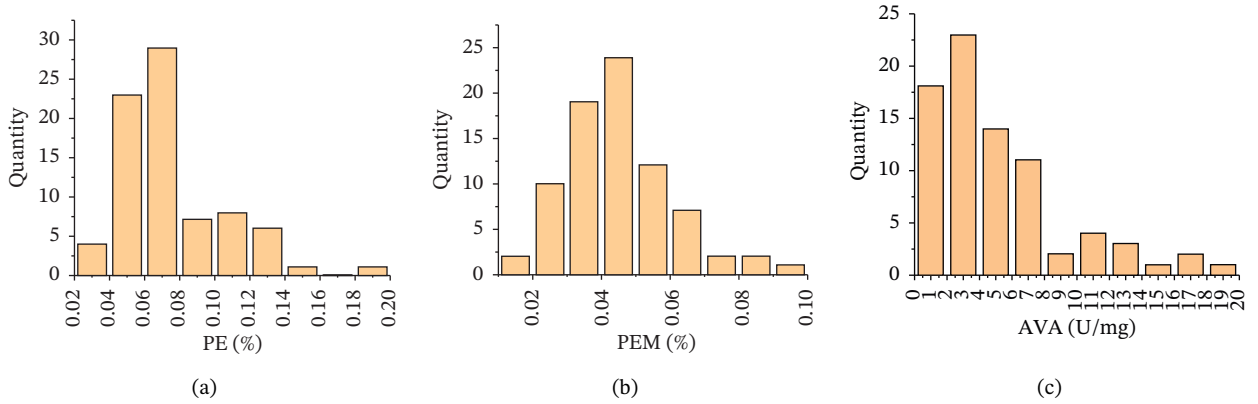


FIGURE 1 | Distribution of PE (%), PEM (%), and AVA (U/mg) in *Fritillaria thunbergii* samples. (a) Frequency distribution plot of PE content in samples; (b) frequency distribution plot of PEM content in samples; (c) frequency distribution plot of AVA in samples.

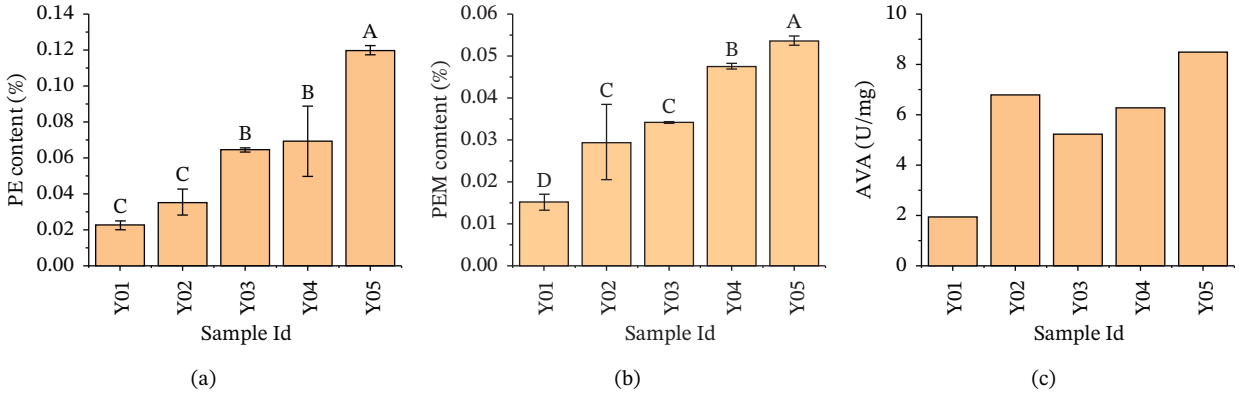


FIGURE 2 | Characterization of PE/PEM content and AVA in *Fritillaria thunbergii* Miq. under different processing methods. (a) PE content in *Fritillaria thunbergii* under different processing methods; (b) PEM content in *Fritillaria thunbergii* under different processing methods; (c) AVA in *Fritillaria thunbergii* under different processing methods. Samples Y01–Y05 correspond to shell powder–processed *Fritillaria thunbergii*, sulfur-processed *Fritillaria thunbergii*, slice-dried *Fritillaria thunbergii*, little-complete-dried *Fritillaria thunbergii*, and freeze-dried *Fritillaria thunbergii*. Different uppercase letters indicate statistically significant differences ($p < 0.05$).

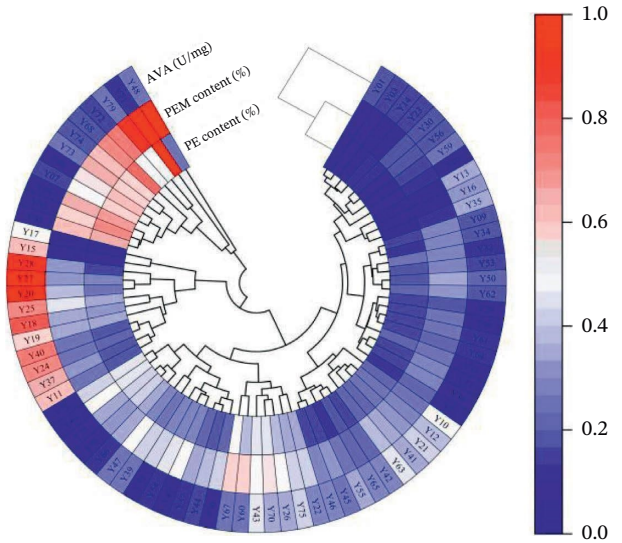


FIGURE 3 | Cluster analysis diagram based on PE, PEM, and AVA results. Indicator for content/activity levels: red: high content (PE/PEM) or high activity (AVA); blue: low content (PE/PEM) or low activity (AVA).

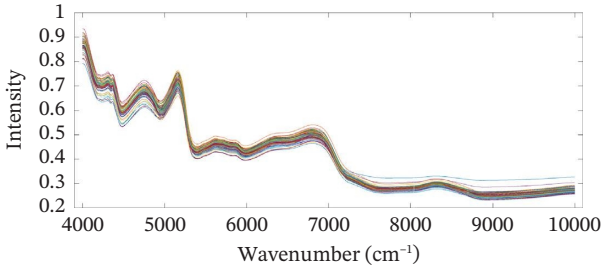


FIGURE 4 | Raw NIR spectra from the whole experiment of 79 *Fritillaria thunbergii* samples.

was observed between PE/PEM and AVA. Samples with high PE/PEM content (Y01, Y05, Y06, Y07, Y08, Y48, Y71, Y72, Y73, Y74) and those with high AVA (Y11, Y15, Y17, Y18, Y19, Y20, Y24, Y25, Y27, Y28, Y37, Y40) clustered into distinct groups, respectively.

3.4 | NIR Spectral Features and Selection of the Preprocessing Methods

Figure 4 displays the raw NIR spectra of 79 *F. thunbergii* samples in the wavenumber region of 4000–10000 cm^{-1}. Within this region, the NIR spectra exhibit several prominent absorption peaks corresponding to specific molecular vibrations, including: Combination vibrations of C–H and C–C bonds (4000 cm^{-1}), second overtone of carbonyl groups (5350 cm^{-1}), first overtone of O–H and N–H bonds (6900 cm^{-1}) and stretching. Asymmetric stretching and asymmetric deformation vibrations of C–H bonds (7200 cm^{-1}). These bands likely reflect the steroidal alkaloid backbone, carbonyl/ester groups in alkaloids, polysaccharides/water content, and fatty acid chains/alkaloid side chains in *F. thunbergii*, respectively. The raw NIR spectra of all samples were highly similar, making direct differentiation challenging. Consequently, spectral preprocessing is crucial for enhancing spectral quality. Six preprocessing methods were compared, with results summarized in Table 2. The PLS model utilizing first derivative + multiplicative scatter correction (MSC) preprocessing demonstrated the highest accuracy in determining PE/PEM contents and AVA. Therefore, PLS quantitative models were constructed based on first derivative + MSC preprocessed spectral data.

3.5 | Optimal Wavelength Selection

Typically, full-spectrum NIR data contain redundant variables with multicollinearity, complicating model development. Feature wavelength selection is therefore critical. We compared two established algorithms: Si-PLS and CARS.

3.5.1 | Results of Si-PLS Models

For the Si-PLS model of PE, the number of intervals was set to 10, and intervals 2, 4, 7, and 8 were selected. For the Si-PLS model of PEM, the number of intervals was set to 30, with intervals 4, 21, 22, and 27 selected. For the Si-PLS model of AVA, the number of

TABLE 2 | Comparison of different spectral preprocessing methods on performance of PLS calibration models.

Properties	Methods	PLS results								
		R_C^2	RMSEC	RPDC	R_P^2	RMSEP	RPD	R_{CV}^2	RMSECV	nL
PE	Original	0.8120	0.0119	2.3273	0.5791	0.0286	2.2031	0.6534	0.0173	11
	First derivative	0.9033	0.0093	3.2240	0.6644	0.0209	2.3958	0.5486	0.0204	5
	MSC	0.5801	0.0202	1.5574	0.3418	0.0187	1.2591	0.3176	0.0398	7
	SNV	0.5903	0.0199	1.5767	0.5169	0.0177	1.4696	0.3413	0.0269	7
	First derivative + MSC	0.9254	0.0084	3.6956	0.8180	0.0124	2.6528	0.8127	0.0107	5
	First derivative + SNV	0.9488	0.0061	4.4601	0.5634	0.0272	2.2803	0.5814	0.0153	5
PEM	Original	0.8121	0.0131	3.2168	0.5724	0.0123	2.1976	0.2717	0.0135	8
	First derivative	0.8437	0.0056	2.5525	0.5293	0.0154	2.1636	0.6444	0.0048	4
	MSC	0.4085	0.0123	1.3122	0.3140	0.0225	1.0852	0.5805	0.0061	9
	SNV	0.3654	0.0124	1.2669	0.3059	0.0222	1.2261	0.5054	0.0108	9
	First derivative + MSC	0.9224	0.0044	3.6227	0.7538	0.0116	2.2708	0.4750	0.0068	5
	First derivative + SNV	0.8890	0.0049	3.0287	0.4207	0.0181	2.1571	0.5599	0.0045	4
AVA	Original	0.8578	3.3017	1.7253	0.6028	3.3760	1.6207	0.5157	0.7392	10
	First derivative	0.8301	2.2474	2.4485	0.6601	3.1484	1.5402	0.6435	1.6977	4
	MSC	0.7414	2.3413	1.9847	0.5374	4.9004	1.5019	0.4084	0.8769	10
	SNV	0.5569	3.7342	1.5161	0.5425	3.6910	1.5103	0.4889	2.2508	8
	First derivative + MSC	0.8824	1.5347	3.6230	0.8017	2.8371	2.4927	0.7923	0.8007	5
	First derivative + SNV	0.8964	1.7470	3.1354	0.3727	4.6303	1.2898	0.6700	1.7287	4

intervals was set to 30, with intervals 4, 10, 12, and 20 selected. These configurations yielded the best prediction results (Supporting Figure S2). However, compared to the full-spectrum PLS models, the predictive performance of the Si-PLS models was not necessarily superior (Table 3). The Si-PLS model for PE achieved an R_P^2 of 0.8268, and the Si-PLS model for PEM achieved an R_P^2 of 0.7883, both slightly better than their respective full-spectrum PLS models. In contrast, the Si-PLS model for AVA achieved an R_P^2 of 0.7795, which was lower than its full-spectrum PLS model. This occurred because variable selection, while eliminating unnecessary spectral bands, may also remove useful spectral information.

3.5.2 | Results of CARS-PLS Models

During CARS execution, Monte Carlo sampling was set to 100 iterations, with 80% of samples randomly selected in each iteration to construct PLS models. The wavelength selection and distribution for PE, PEM, and AVA via CARS are presented in supporting figure S3. The number of sampled variables decreased sharply with increasing sampling iterations and gradually stabilized (Supporting Figure S3 A, C, E). This occurs because the EDF eliminated numerous irrelevant wavelengths, while ARS retained variables with larger absolute regression coefficients. The RMSECV varied across iterations, with its minimum value (indicated by blue asterisks) typically marking the optimal variable subset. Ultimately, CARS selected 41, 44, and 113 wavelength variables for PE, PEM, and AVA, respectively (Supporting Table S2). These optimal variables, highlighted by red circles on raw spectra (Supporting Figure S3 B, D, F), enable clearer visualization.

The CARS-PLS models built with these optimal variables yielded the following results (Table 3): PE model: $R_P^2 = 0.8850$, RMSEP decreased from 0.0124% to 0.0101%; PEM model: $R_P^2 = 0.8240$, RMSEP decreased from 0.0116% to 0.0070%; AVA model: $R_P^2 = 0.8336$, RMSEP decreased from 2.8371 U/mg to 1.7921 U/mg. All RPD values exceeded 2.4, confirming robust predictive capability. Figure 5 displays the fitting plots of training versus test sets for PE, PEM, and AVA CARS-PLS models.

TABLE 3 | Comparison of results obtained by different wavelength selection methods on PE, PEM, and AVA.

Properties	Methods	PLS results					
		R_C^2	RMSEC	RPDC	R_P^2	RMSEP	RPD
PE	Full-PLS	0.9254	0.0084	3.6956	0.818	0.0124	2.6528
	CRAS-PLS	0.9444	0.0071	4.2812	0.8850	0.0101	3.0120
	Si-PLS	0.9137	0.0084	3.4351	0.8268	0.0123	2.4546
PEM	Full-PLS	0.9224	0.0044	3.6227	0.7538	0.0116	2.2708
	CRAS-PLS	0.9620	0.0029	5.1770	0.8240	0.0070	2.4351
	Si-PLS	0.9204	0.0042	3.6196	0.7883	0.0077	2.2203
AVA	Full-PLS	0.8824	1.5347	3.623	0.8017	2.8371	2.4927
	CRAS-PLS	0.9156	1.1723	3.4731	0.8336	1.7921	2.5041
	Si-PLS	0.8912	1.3744	3.0591	0.7795	1.7194	2.1569

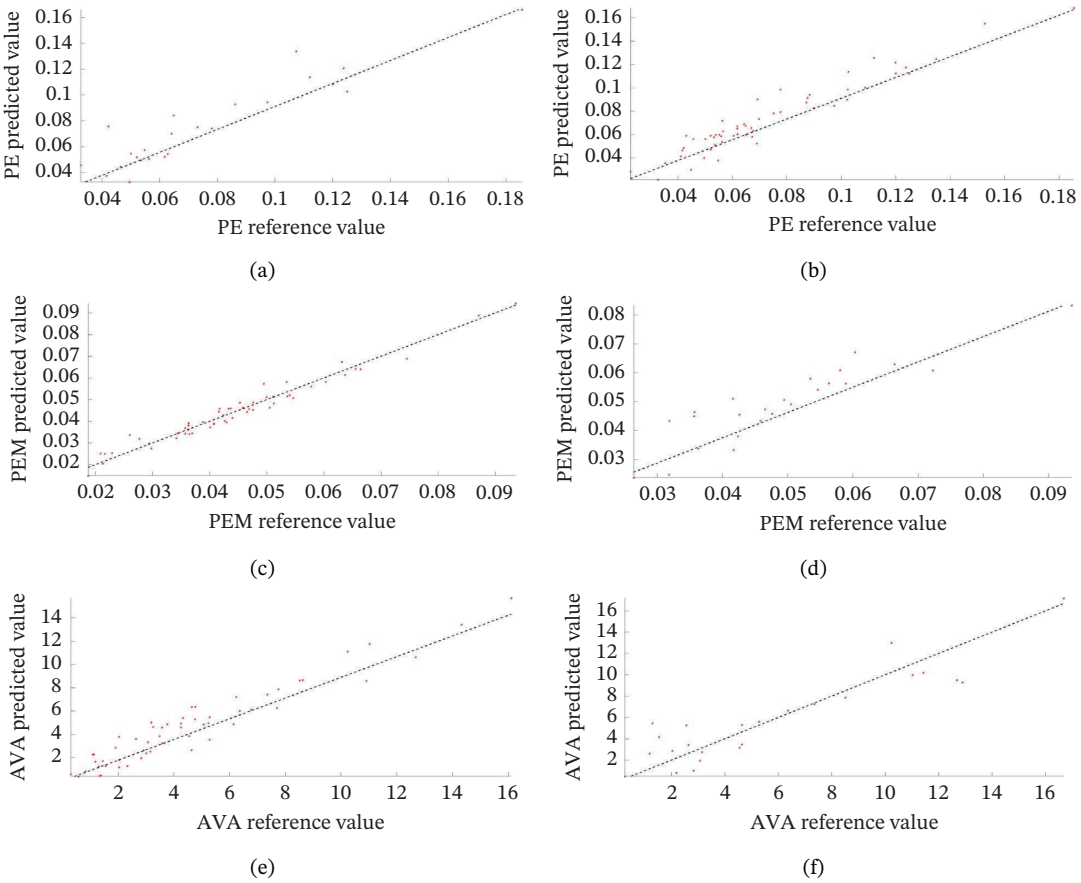


FIGURE 5 | Fitting plots of training versus test sets for PE, PEM, and AVA CARS-PLS models. (a), (c), (e) Fitting plots of the training set for PE, PEM, and AVA CARS-PLS models, respectively; (b), (d), (f) fitting plots of the test set for PE, PEM, and AVA CARS-PLS models, respectively.

4 | Discussion

4.1 | Effects of Processing Methods on the Composition and Pharmacological Efficacy of FTB

In this study, we demonstrated that different processing methods alter the PE and PEM content in FTB. Specifically, sulfur-processed *F. thunbergii* and shell powder-processed *F. thunbergii* exhibited contents below pharmacopoeial standards. The shell powder abrasion followed by sun-drying represents the oldest processing technique and is still utilized by some traditional Chinese medicine practitioners. Sulfur fumigation is employed for pest and mold prevention under suboptimal storage conditions [23]. Presents potential safety hazards and quality issues. This method has been shown to alter the composition of saponins and alkaloids [24], with significant changes in water-soluble constituents postfumigation [25]. Modern storage facilities with temperature control enable sulfur-free processing. The current mainstream methods involve direct drying of small bulbs and fresh-slicing followed by drying for larger bulbs. Freeze-drying, recognized for superior retention of bioactive components, was also investigated. The total PE/PEM content (%) across processing types was quantified as follows: freeze-dried *F. thunbergii*: 0.1735%; little-complete-dried *F. thunbergii*: 0.1168%; slice-dried *F. thunbergii*: 0.0985%; sulfur-processed *F. thunbergii:* 0.0647%; shell powder-processed *F. thunbergii:* 0.0377%.

Alterations in processing methods not only induce compound transformation in *F. thunbergii* but also modify the proportion and content of bioactive constituents. The specific conditions of these transformations and their impact on pharmacological efficacy remain uncertain [26]. Relying solely on PE and PEM content for quality assessment raises concerns regarding its validity. Consequently, we evaluated the AVA across differently processed samples. The shell powder-processed samples exhibited significantly lower AVA, less than half that of other methods, while the remaining four processing types (freeze-dried, little-complete-dried, slice-dried, and sulfur-processed *F. thunbergii*) consistently demonstrated AVA >4 U/mg. Integrated results indicate that freeze-dried, little-complete-dried, slice-dried, and sulfur-processed *F. thunbergii* represent superior processing approaches for production regions.

4.2 | Correlation Between PE/PEM Content and AVA

FTB is a commonly employed medicinal material in traditional Chinese formulations for viral influenza treatment [1]. However, research on its AVA remains relatively scarce. Huang et al. [27] demonstrated that PEM inhibits MEK/ERK phosphorylation, thereby reducing cardiomyocyte apoptosis, inflammatory responses, and fibrosis in coxsackievirus B-induced viral myocarditis. Kim et al. [7, 10] reported that *F. thunbergii* extract exhibits potent antiviral effects both in vitro and in vivo with a superior safety profile compared to oseltamivir. Network pharmacology analyses suggest β-sitosterol and pelargonin as potential contributors to this activity [28], though the precise mechanism remains unclear. Notably, β-sitosterol and

pelargonin occur at trace levels in FTB, and our study found no significant correlation between PE/PEM content and AVA. This indicates that AVA likely arises from the synergistic effects of multiple bioactive components, aligning with the holistic theory of traditional Chinese medicine.

4.3 | Impact of Spectral Preprocessing on Quantitative Accuracy in *F. thunbergii*

Spectral preprocessing enhances the accuracy of determination results affected by multiple interference factors (e.g., background noise, instrumental variations, and particle size/shape differences) [29]. In this study, the PLS model employing first-derivative + MSC preprocessing demonstrated superior performance in determining PE/PEM contents and AVA. First-derivative preprocessing effectively minimizes peak overlap while eliminating constant and linear baseline drift [17]. Guo et al. [30] observed enhanced prominence of characteristic spectral bands with increasing derivative orders. However, standalone derivative methods may amplify noise and reduce signal-to-noise ratios (SNR). As evidenced by Hao et al. [17], raw spectra without preprocessing yielded better XO inhibitory activity PLS models. Thus, first-derivative is typically combined with complementary techniques. MSC separates scattering signals from absorption signals using a uniform scattering coefficient, effectively mitigating spectral variations caused by differential scattering levels and strengthening spectral-data correlations [16]. Its synergy with the first derivative is well established. Postpreprocessing, model R_P^2 values for PE, PEM, and AVA increased by 0.2389, 0.1814, and 0.1989, respectively, versus raw data. The robust linearity of AVA models indicates substantial chemical basis for antiviral efficacy. Conversely, the insignificant correlation between AVA and PE/PEM content suggests additional bioactive constituents contribute to antiviral effects in *F. thunbergii*.

4.4 | Application of PE/PEM and AVA CARS-PLS Quantitative Models

Previous studies have explored various optical techniques for the quality evaluation of FTB. Laser-induced breakdown spectroscopy (LIBS) has demonstrated significant potential in elemental analysis and adulteration detection. For instance, LIBS combined with the LASSO-PLSR-SVR model achieved a remarkably high coefficient of determination ($R^2 = 0.9983$) for detecting the adulteration of *F. thunbergii* in *Fritillaria cirrhosa* [31]. Furthermore, LIBS coupled with machine learning algorithms (e.g., GBM, SVR, and BPNN) has been successfully applied for the rapid quantification of heavy metals (Cd, Cu, and Pb) in FTB, offering a swift solution for safety monitoring [32, 33]. However, LIBS is a micro-destructive technique primarily sensitive to atomic emissions, which may limit its direct application for holistic organic compound quantification compared to vibrational spectroscopy.

On the other hand, hyperspectral imaging (HSI) has been utilized for visualizing chemical component distribution and variety discrimination in FTB. Recent research integrating HSI with convolutional neural networks (CNN) achieved a training accuracy of 98.88% for distinguishing FTB varieties [34]. Similarly, HSI combined with chemometrics successfully visualized the content of PE and PEM in sulfur-fumigated bulbs, with prediction correlation coefficients (r_p) exceeding 0.8 [12]. While HSI provides valuable spatial information, its high data dimensionality and complex instrumentation can lead to substantial computational costs.

In contrast, the NIRS method proposed in this study offers a balance between spectral resolution and rapid data acquisition. Our NIR-based CARS-PLS quantitative models for PE, PEM, and AVA achieved test set prediction coefficients (R_P^2) of 0.8850, 0.8240, and 0.8336, respectively. These results are comparable to or slightly better than those obtained using HSI, thereby providing a potentially simpler and more cost-effective solution for routine quality control.

5 | Conclusions

This study proposed a rapid analytical method based on NIRS to evaluate the quality and AVA of *F. thunbergii* subjected to different processing methods. After confirming the feasibility of the PLS method, various spectroscopic preprocessing and wavelength selection techniques were extensively investigated and compared to construct the optimal NIRS models.

The experimental results indicated that appropriate spectral preprocessing algorithms (first-derivative combined with MSC) and wavelength selection techniques (CARS) significantly improved the prediction accuracy of the constituent content models. Our NIR-based CARS-PLS quantitative models for PE, PEM, and AVA achieved test set prediction coefficients (R_P^2) of 0.8850, 0.8240, and 0.8336, respectively. Concurrently, the RMSEP decreased significantly, and all models exhibited RPD values greater than 2.4, demonstrating good model stability. This confirmed the model's ability to accurately predict the content of PE/PEM and AVA in *F. thunbergii*. Furthermore, the study revealed that the freeze-drying method optimally preserved the active compounds (total PE/PEM content of 0.1735%) and AVA (8.517 U/mg), whereas traditional sulfur fumigation led to a significant decline in quality.

The findings of this study demonstrate the feasibility of using NIRS analysis to comprehensively predict the quality and efficacy of *F. thunbergii* from a chemical composition perspective. Although based on a limited number of reference samples, these results represent a promising initial step toward the practical application of this methodology in the quality control and efficacy assessment of *F. thunbergii* processing. NIRS serves as a non-invasive, cost-effective, and rapid alternative to tedious conventional chemical analyses. This presents a viable opportunity for traditional Chinese medicine manufacturers to conduct swift screening of large batches of their products. However, it should be noted that the quality of *F. thunbergii* is also influenced by factors such as species, origin, cultivation management, and storage conditions. Therefore, further efforts are required to expand the sample size to enhance the performance and generalizability of the model, thereby contributing a wealth of knowledge to the standardized management of traditional Chinese medicines.

Author Contributions

J.S.: conceptualization and writing–review and editing; H.L.: methodology and writing–original draft preparation; C.W.: software; M.Z.:

validation; L.C.: formal analysis; Z. W.: supervision and funding acquisition; A.L. and Q.S.: visualization; J.J.: project administration.

Acknowledgments

At the same time, we declare that Google Gemini 3 Pro was used solely for the purpose of translating and refining the English language of this manuscript. The authors reviewed and edited the output as needed and take full responsibility for the content of the publication. We further declare that no artificial intelligence tools were used to manipulate or generate any experimental data or results.

Funding

This research was supported by the National Key Research and Development Program of China (2022YFC3501504); Key project at central government level: The Ability Establishment of Sustainable Use for Valuable Chinese Medicine Resources (2060302); Key Scientific and Technological Grant of Zhejiang, China for Breeding New Agricultural Varieties (2021C02074); Legacy and innovation of State Administration of Traditional Chinese Medicine, China (GZY-KJS-2021–020); The "San Nong Jiu Fang" Science, Technology Cooperation Project of Zhejiang Province (2025SNJF078).

Disclosure

The funding bodies supporting this research had no direct influence on the scientific investigation reported in this study, which was carried out as independent research. Although some authors are affiliated with Zhejiang Research Institute of Traditional Chinese Medicine Co., Ltd., this company had no role in the design of the study; in the collection, analyses, or interpretation of data; in the writing of the manuscript; or in the decision to publish the results.

Conflicts of Interest

The authors declare no conflicts of interest.

Data Availability Statement

Data are available on request from the authors.

References

1. H. Li, A. Hung, M. Li, and A. W. H. Yang, "*Fritillariae thunbergii* Bulbus: Traditional Uses, Phytochemistry, Pharmacodynamics, Pharmacokinetics and Toxicity," *International Journal of Molecular Sciences* 20, no. 7 (2019): 1667, https://doi.org/10.3390/ijms20071667.

2. S. H. Nile, J. Su, D. Wu, et al., "*Fritillaria thunbergii* Miq. (Zhe Beimu): A Review on Its Traditional Uses, Phytochemical Profile and Pharmacological Properties," *Food and Chemical Toxicology* 153 (2021): 112289, https://doi.org/10.1016/j.fct.2021.112289.

3. C. He, X. Liu, Y. Liu, J. Wang, and D. Chen, "A New Alkaloid With Cytotoxic Activity From *Fritillaria thunbergii* Miq," *Natural Product Research* 36, no. 20 (2022): 5297–5303, https://doi.org/10.1080/14786419.2021.1933970.

4. S. Feng, G. Xu, Q. Ding, and Y. Shi, "*Fritillaria thunbergii* Miq. Extract Ameliorated Experimental Pulmonary Fibrosis Partly Through the PI3K/AKT/FOXO Signalling Pathway," *Journal of Ethnopharmacology* 343 (2025): 119445, https://doi.org/10.1016/j.jep.2025.119445.

5. X. Li, P. Wang, Y. Tong, J. Liu, and G. Shu, "UHPLC-Q-Exactive Orbitrap MS/MS-Based Untargeted Metabolomics and Molecular Networking Reveal the Differential Chemical Constituents of the Bulbs and Flowers of *Fritillaria thunbergii*," *Molecules* 27, no. 20 (2022): 6944, https://doi.org/10.3390/molecules27206944.

6. S. W. Chan, in *Pharmacological and Chemical Investigations into Bulbus fritillariae* (Chinese University of Hong Kong, 2000), Ph.D. Thesis.

7. E. J. Kim, Y. P. Yoon, K. W. Woo, et al., "Verticine, Ebeiedine and Suchengbeisine Isolated From the Bulbs of *Fritillaria thunbergii* Miq. Inhibited the Gene Expression and Production of MUC5AC Mucin From Human Airway Epithelial Cells," *Phytomedicine* 23, no. 2 (2016): 95–104, https://doi.org/10.1016/j.phymed.2015.12.016.

8. J. Xu, W. Zhao, L. Pan, et al., "Peimine, A Main Active Ingredient of *Fritillaria*, Exhibits Anti-Inflammatory and Pain Suppression Properties at the Cellular Level," *Fitoterapia* 111 (2016): 1–6, https://doi.org/10.1016/j.fitote.2016.03.018.

9. M. Zhu, W. Xu, J. Jiang, et al., "Peiminine Suppresses RANKL-Induced Osteoclastogenesis by Inhibiting the NFATc1, ERK, and NF-κB Signaling Pathways," *Frontiers in Endocrinology* 12 (2021): 736863, https://doi.org/10.3389/fendo.2021.736863.

10. M. Kim, D. V. Nguyen, Y. Heo, K. H. Park, H. D. Paik, and Y. B. Kim, "Antiviral Activity of *Fritillaria thunbergii* Extract Against Human Influenza Virus H1N1 (PR8) in Vitro, in Ovo and in Vivo," *Journal of Microbiology and Biotechnology* 30, no. 2 (2020): 172–177, https://doi.org/10.4014/jmb.1908.08001.

11. S. L. Li, G. Lin, S. W. Chan, and P. Li, "Determination of the Major Isosteroidal Alkaloids in Bulbs of Fritillaria by High-Performance Liquid Chromatography Coupled With Evaporative Light Scattering Detection," *Journal of Chromatography A* 909, no. 2 (2001): 207–214, https://doi.org/10.1016/s0021-9673(00)01083-9.

12. J. He, Y. He, and A. C. Zhang, "Determination and Visualization of Peimine and Peiminine Content in *Fritillaria thunbergii* Bulbi Treated by Sulfur Fumigation Using Hyperspectral Imaging With Chemometrics," *Molecules* 22, no. 9 (2017): 1402, https://doi.org/10.3390/molecules22091402.

13. Y. K. Lin, Y. L. Ho, Y. Zhao, and Y. S. Chang, "Quality Assessment of *Fritillariae thunbergii* Bulbus Sold in Taiwan Markets Using a Validated HPLC-UV Method Combined With Hierarchical Clustering Analysis," *Journal of Food and Drug Analysis* 23, no. 1 (2015): 130–135, https://doi.org/10.1016/j.jfda.2014.06.004.

14. K. B. Beć, J. Grabska, and C. W. Huck, "Miniaturized NIR Spectroscopy in Food Analysis and Quality Control: Promises, Challenges, and Perspectives," *Foods* 11, no. 10 (2022): 1465, https://doi.org/10.3390/foods11101465.

15. Y. Wang, L. Xing, H. J. He, J. Zhang, K. W. Chew, and X. Ou, "NIR Sensors Combined With Chemometric Algorithms in Intelligent Quality Evaluation of Sweetpotato Roots from 'Farm' to 'Table': Progresses, Challenges, Trends, and Prospects," *Food Chemistry X* 22 (2024): 101449, https://doi.org/10.1016/j.fochx.2024.101449.

16. W. J. Du, C. Y. Wu, H. E. Yu, Q. R. Kong, Y. Xu, and W. Zhang, "Determination of Multicomponents in Rubi Fructus by Near-Infrared Spectroscopy Technique," *International Journal of Analytical Chemistry* 2023 (2023): 1–9, https://doi.org/10.1155/2023/5575944.

17. J. W. Hao, N. D. Chen, X. X. Fan, et al., "Rapid Determination of Total Flavonoid Content, Xanthine Oxidase Inhibitory Activities, and Antioxidant Activity in *Prunus mume* by Near-Infrared Spectroscopy," *Journal of Pharmacy Biomedicine Analytical* 246 (2024): 116164, https://doi.org/10.1016/j.jpba.2024.116164.

18. S. Zhang, X. Gong, and H. Qu, "Near-Infrared Spectroscopy and HPLC Combined With Chemometrics for Comprehensive Evaluation of Six Organic Acids in Ginkgo biloba Leaf Extract," *Journal of Pharmacy and Pharmacology* 74, no. 7 (2022): 1040–1050, https://doi.org/10.1093/jpp/rgab177.

19. W. He, H. Han, W. Wang, and B. Gao, "Anti-Influenza Virus Effect of Aqueous Extracts From Dandelion," *Virology Journal* 8, no. 1 (2011): 538, https://doi.org/10.1186/1743-422x-8-538.

20. X. Y. Shi, X. Q. Gan, X. B. Wang, et al., "Rapid Detection of Ganoderma lucidum Spore Powder Adulterated With Dyed Starch by NIR Spectroscopy and Chemometrics," *Lebensmittel-Wissenschaft and Technologie* 167 (2022): 113829, https://doi.org/10.1016/j.lwt.2022.113829.

21. C. B. Wang, H. S. Li, M. D. Zhang, Z. A. Wang, Q. S. Shao, and J. Sun, "Quality Assessment of Differentially Processed Rubi Fructus (Rubus

chingii Hu.) Using Near-Infrared Spectroscopy and HPLC," *Lebensmittel-Wissenschaft and Technologie* 235 (2025): 118580, https://doi.org/10.1016/j.lwt.2025.118580.

22. Z. W. Lan, Y. F. Zhang, Y. Zhang, et al., "Rapid Evaluation on Pharmacodynamics of Curcumae Rhizoma Based on Micro-NIR and Benchtop-NIR," *Journal of Pharmacy Biomedicine Analytical* 200 (2021): 114074, https://doi.org/10.1016/j.jpba.2021.114074.

23. D. E. L. T. C. Chen, "Experiment on Processing *Fritillaria thunbergii* by Sulfur Fumigation," *China Journal of Chinese Materia Medica* 10 (1985): 19–21.

24. H. J. Li, Y. Jiang, and P. Li, "Chemistry, Bioactivity and Geographical Diversity of Steroidal Alkaloids From the Liliaceae Family," *Natural Product Reports* 23, no. 5 (2006): 735–752, https://doi.org/10.1039/b609306j.

25. W. F. Y. Du, K.X., and T. Zhu, "HPLC-ESI-MS Fingerprint Analysis of Thunberg Fritillary Bulb in Different Producing Areas," *China Journal of Traditional Chinese Medicine and Pharmacy* 31 (2016): 4956–4960.

26. Y. H. Shi, Q. W. Huang, S. M. Zhu, et al., "Chemical Profiling of *Fritillariae thunbergii* Miq Prepared by Different Processing Methods Reveals Two New Quality Markers: Zhebeininoside and Imperialine-3-β-D-Glucoside," *Journal of Ethnopharmacology* 283 (2022): 114670, https://doi.org/10.1016/j.jep.2021.114670.

27. Y. P. Huang, H. L. Xiao, Y. H. Li, and J. J. Li, "Effects of Verticinone on Myocardial Apoptosis and Inflammation in Neonatal Mice With Coxsackievirus B-Induced Myocarditis by Inhibiting MEK/ERK Phosphorylation," *Pharmacology and Clinics of Chinese Materia Medica* 36 (2020): 94–99.

28. M. Kim and Y. B. Kim, "A Network-Based Pharmacology Study of Active Compounds and Targets of *Fritillaria thunbergii* Against Influenza," *Computational Biology and Chemistry* 89 (2020): 107375, https://doi.org/10.1016/j.compbiolchem.2020.107375.

29. S. Liu, S. Wang, C. Hu, D. Kong, and Y. Yuan, "Series Fusion of Scatter Correction Techniques Coupled With Deep Convolution Neural Network as a Promising Approach for NIR Modeling," *Spectrochimica Acta Part A: Molecular and Biomolecular Spectroscopy* 291 (2023): 122371, https://doi.org/10.1016/j.saa.2023.122371.

30. J. Guo, K. F. Zhou, J. L. Wang, et al., "Estimation of Rock Copper Content Based on Fractional-Order Derivative and Visible Near-Infrared-Shortwave Infrared Spectroscopy," *Ore Geology Reviews* 150 (2022): 105090, https://doi.org/10.1016/j.saa.2023.122371.

31. K. Wei, G. Teng, Q. Q. Wang, et al., "Rapid Test for Adulteration of *Fritillaria thunbergii* in *Fritillaria cirrhosa* by Laser-Induced Breakdown Spectroscopy," *Foods* 12, no. 8 (2023): 1710, https://doi.org/10.3390/foods12081710.

32. M. H. Kabir, M. L. Guindo, R. Chen, X. Luo, W. Kong, and F. Liu, "Heavy Metal Detection in *Fritillaria thunbergii* Using Laser-Induced Breakdown Spectroscopy Coupled With Variable Selection Algorithm and Chemometrics," *Foods* 12, no. 6 (2023): 1125, https://doi.org/10.3390/foods12061125.

33. X. M. Luo, R. Q. Chen, M. H. Kabir, et al., "Fast Detection of Heavy Metal Content in *Fritillaria thunbergii* by Laser-Induced Breakdown Spectroscopy With PSO-BP and SSA-BP Analysis," *Molecules* 28, no. 8 (2023): 3360, https://doi.org/10.3390/molecules28083360.

34. M. H. Kabir, M. L. Guindo, R. Chen, F. Liu, X. Luo, and W. Kong, "Deep Learning Combined With Hyperspectral Imaging Technology for Variety Discrimination of *Fritillaria thunbergii*," *Molecules* 27, no. 18 (2022): 6042, https://doi.org/10.3390/molecules27186042.

Supporting Information

Additional supporting information can be found online in the Supporting Information section. *(Supporting Information)* Supporting Information. The supporting documents present the processing flowchart of *F. thunbergii*, the original data obtained through chemical detection, the selected spectral intervals for the optimal Si-PLS model, and the wavelength selection profiles of CARS for PE, PEM, and AVA, as well as the specific wavelength variables selected by the CARS algorithm for PE, PEM, and AVA.